

## Special Section:

ExoMars Trace Gas Orbiter -  
One Martian Year of Science

## Key Points:

- We present that density around 90 and 140 km and temperature around 80 km of Mars atmosphere can be retrieved from OI 557.7 nm dayglow
- Density around 90 and 140 km increases around perihelion periods, which can be explained by temperature variation in the lower atmosphere
- Temperature around 80 km is higher than predicted by general circulation models

## Correspondence to:

S. Aoki,  
[shohei.aoki@edu.k.u-tokyo.ac.jp](mailto:shohei.aoki@edu.k.u-tokyo.ac.jp)












## Citation:

Aoki, S., Gkouvelis, L., Gérard, J.-C., Soret, L., Hubert, B., Lopez-Valverde, M. A., et al. (2022). Density and temperature of the upper mesosphere and lower thermosphere of Mars retrieved from the OI 557.7 nm dayglow measured by TGO/NOMAD. *Journal of Geophysical Research: Planets*, 127, e2022JE007206. <https://doi.org/10.1029/2022JE007206>

Received 25 JAN 2022

Accepted 23 MAY 2022

# Density and Temperature of the Upper Mesosphere and Lower Thermosphere of Mars Retrieved From the OI 557.7 nm Dayglow Measured by TGO/NOMAD

S. Aoki<sup>1,2,3</sup> , L. Gkouvelis<sup>3,4</sup> , J.-C. Gérard<sup>3</sup>, L. Soret<sup>3</sup> , B. Hubert<sup>3</sup>, M. A. Lopez-Valverde<sup>5</sup> , F. González-Galindo<sup>5</sup> , H. Sagawa<sup>6</sup> , I. R. Thomas<sup>2</sup> , B. Ristic<sup>2</sup> , Y. Willame<sup>2</sup>, C. Depiesse<sup>2</sup> , J. Mason<sup>7</sup>, M. R. Patel<sup>7</sup> , G. Bellucci<sup>8</sup>, J.-J. Lopez-Moreno<sup>5</sup>, F. Daerden<sup>2</sup> , and A. C. Vandaele<sup>2</sup>

<sup>1</sup>Department of Complexity Science and Engineering, Graduate School of Frontier Sciences, The University of Tokyo, Kashiwa, Japan, <sup>2</sup>Royal Belgian Institute for Space Aeronomy, Brussels, Belgium, <sup>3</sup>LPAP, STAR Institute, Université de Liège, Liège, Belgium, <sup>4</sup>NASA/Ames Research Center, Moffet Field, Mountain View, CA, USA, <sup>5</sup>Instituto de Astrofísica de Andalucía-CSIC, Glorieta de la Astronomía, Granada, Spain, <sup>6</sup>Faculty of Science, Kyoto Sangyo University, Kamigamo Motoyama, Kyoto, Japan, <sup>7</sup>School of Physical Sciences, The Open University, Milton Keynes, UK, <sup>8</sup>Istituto di Astrofisica e Planetologia Spaziali, Roma, Italy

**Abstract** The upper mesosphere and lower thermosphere of Mars (70–150 km) is of high interest because it is a region affected by climatological/meteorological events in the lower atmosphere and external solar forcing. However, only a few measurements are available at this altitude range. OI 557.7 nm dayglow emission has been detected at these altitudes by the limb observations with Nadir and Occultation for Mars Discovery (NOMAD) aboard the ExoMars Trace Gas Orbiter (TGO). We develop an inversion method to retrieve density and temperature at these altitudes from the OI 557.7 nm dayglow limb profiles. We demonstrate that the atmospheric density around 90 and 140 km and temperature around 80 km during the daytime can be retrieved from the TGO/NOMAD limb measurements. The retrieved densities show a large seasonal variation both around 90 and 140 km and reach maximum values around perihelion period. This can be explained by temperature variation in the lower atmosphere driven by the dust content and Sun-Mars distance. Temperature around 80 km is higher than predicted by general circulation models, which is tentatively consistent with the warm atmospheric layer recently discovered in nighttime. The temperature retrieval relies on the temperature dependence of the quenching coefficient of <sup>1</sup>S oxygen by CO<sub>2</sub>. Further validation of this coefficient in the range of the Mars upper atmosphere is needed for the verification of the retrieved high temperature.

**Plain Language Summary** Density and thermal structures between 70 and 150 km of Mars atmosphere have not been extensively investigated because these altitudes are too low for in situ measurements by orbiters and too high for general remote-sensing observations. Recently, a bright oxygen dayglow emission with green color (emitted at 557.7 nm) has been found in this altitude range. We combine a detailed photochemical model and widely used inversion scheme to develop a method to obtain density and temperature from the dayglow measurements. With this method, we successfully determine the density around 90 and 140 km, and temperature around 80 km. The densities show clear seasonal variations, with larger values during the southern spring-summer season, stemming from the warmer lower atmosphere, a consequence of the shorter Sun-Mars distance and heating by dust. Temperatures around 80 km are higher than the theoretical predictions. A similar warm atmospheric layer was found in nighttime by previous measurements, and our result suggests that it might also present in daytime. However, further experimental studies on temperature dependence of the related photochemical reactions are needed to firmly confirm the retrieved high temperatures.

## 1. Introduction

The upper mesosphere and lower thermosphere of Mars (hereafter “UMLT”; 70–150 km altitude) is of high interest because this altitudinal region is affected by both climatological/meteorological events in the lower atmosphere (such as dust content variation, atmospheric tides, and waves, etc.) and external events from the space environment (such as solar activity). Understanding of the UMLT climatology driven by these events is important to constrain the escape processes of Mars atmosphere because this region connects the lower and upper

atmospheres. Furthermore, that is also important for future mission planning because Mars orbiters perform aerobraking within this altitude region.

Despite this interest, only a few measurements are available to investigate the climatology of the UMLT region because this altitude range is generally too low for in situ measurements and too high for usual remote-sensing observations. Following several in situ measurements during descent phase of Mars rover/lander missions (e.g., Magalhães et al., 1999; Seiff & Kirk, 1977; Withers & Smith, 2006) and density measurements during aerobraking of Mars orbiters (e.g., Bougher et al., 2017; Keating et al., 1998), Forget et al. (2009) presented the first study of the seasonal variations of the atmospheric density between 60 and 130 km across a full Martian year. These results were based on CO<sub>2</sub> absorption in the UV range measured by stellar occultations performed, mainly during nighttime with the UV spectrometer Spectroscopy for Investigation of Characteristics of the Atmosphere of Mars (SPICAM) aboard Mars Express (MEX). The atmospheric density measured by SPICAM showed a large seasonal fluctuation caused by variations in the dust content of the lower atmosphere (Forget et al., 2009; McDunn et al., 2010; Montmessin et al., 2017). Gröller et al. (2018) performed a similar analysis with Imaging UltraViolet Spectrograph (IUVS) instrument of the Mars Atmosphere and Volatile Evolution (MAVEN) spacecraft. The data set analyzed by Gröller et al. (2018) was based on the dedicated occultation campaigns taken in both night and daytime, which allowed them to investigate the signatures of nonmigrating tides and gravity waves by distinguishing between longitudinal and local time variations. On the other hand, the dedicated occultation campaigns were carried out with an interval of 2 or 3 months, providing only a coarse seasonal coverage. Solar occultation observations from two spectrometers aboard the ExoMars Trace Gas Orbiter (TGO), Nadir and Occultation for Mars Discovery (NOMAD) and Atmospheric Chemistry Suite, are able to measure CO<sub>2</sub> density from the near-surface up to 160 km altitude by observing the infrared CO<sub>2</sub> band (e.g., Starichenko et al., 2021). However, the measurements are limited to the regions over the terminator. Therefore, the climatology of UMLT is still poorly constrained by observations, especially in daytime, because of the lack of the observational coverage.

Recently, the Ultraviolet/visible channel of TGO/NOMAD has discovered the OI 557.7 nm dayglow emission in the UMLT region (Gérard et al., 2020). The emission mechanism of this dayglow is rather simple - this 557.7 nm airglow (sometimes so-called “green light”) is emitted by the electric quadrupole transition of atomic oxygen, from O(<sup>1</sup>S) to O(<sup>1</sup>D) metastable states. Most of the metastable O (<sup>1</sup>S) atoms are produced from photodissociation of CO<sub>2</sub> by EUV solar radiation and Lyman- $\alpha$  (Gkouvelis et al., 2018). This implies that the CO<sub>2</sub> density can be estimated from OI 557.7 nm dayglow emission. Since the OI 557.7 nm dayglow is expected to be present at all of the latitudes/longitudes, this can be a powerful tracer to investigate density and temperature in the UMLT region. Indeed, Gkouvelis, Gérard, González-Galindo, et al. (2020) and Jain et al. (2021) showed that OI dayglow at 297.2 nm taken with MAVEN/IUVS observations, another transition from O(<sup>1</sup>S) to O(<sup>3</sup>P), has a potential to monitor the seasonal variations of the density and temperature around 80 km.

In this study, we develop an inversion method based on the combination between a state-of-the-art photochemical model (Gérard et al., 2019; Gkouvelis et al., 2018; Gkouvelis, Gérard, Ritter et al. (2020); Ritter et al., 2019) and widely used Bayesian algorithm (Rodgers, 2000) in order to retrieve density and temperature in the UMLT region from the OI 557.7 nm dayglow emission measured by TGO/NOMAD. The details of the NOMAD observations and the data set are described in Sections 2. The retrieval method is presented in Section 3.1 and the obtained results are discussed in Section 3.2 and 3.3.

## 2. Observations of the OI 557.7 nm Dayglow by TGO/NOMAD

### 2.1. Data Set – Inertial Limb Observations by TGO/NOMAD

NOMAD, a spectrometer operating in the spectral ranges between 0.2 and 4.3  $\mu\text{m}$  aboard ExoMars TGO (Vandaele et al., 2018), has three spectral channels: a solar occultation channel (SO – Solar Occultation; 2.3–4.3  $\mu\text{m}$ ), a second infrared channel capable of nadir, solar occultation, and limb sounding (LNO – Limb Nadir and solar Occultation; 2.3–3.8  $\mu\text{m}$ ), and an ultraviolet/visible channel (UVIS – Ultraviolet and Visible Spectrometer, 200–650 nm). The UVIS channel has provided spectra of Mars with unprecedented high spectral resolution ( $\sim 1.5$  nm) in the visible domain (Patel et al., 2017; Vandaele et al., 2015), which allows us to investigate new features of the Mars upper atmosphere (López-Valverde et al., 2018). In order to acquire spectra of the upper atmosphere by the UVIS channel, dedicated limb observing modes have been implemented (Gérard et al., 2020). In this study, we analyzed the data set collected in the inertial pointing mode. Figure 1a shows the

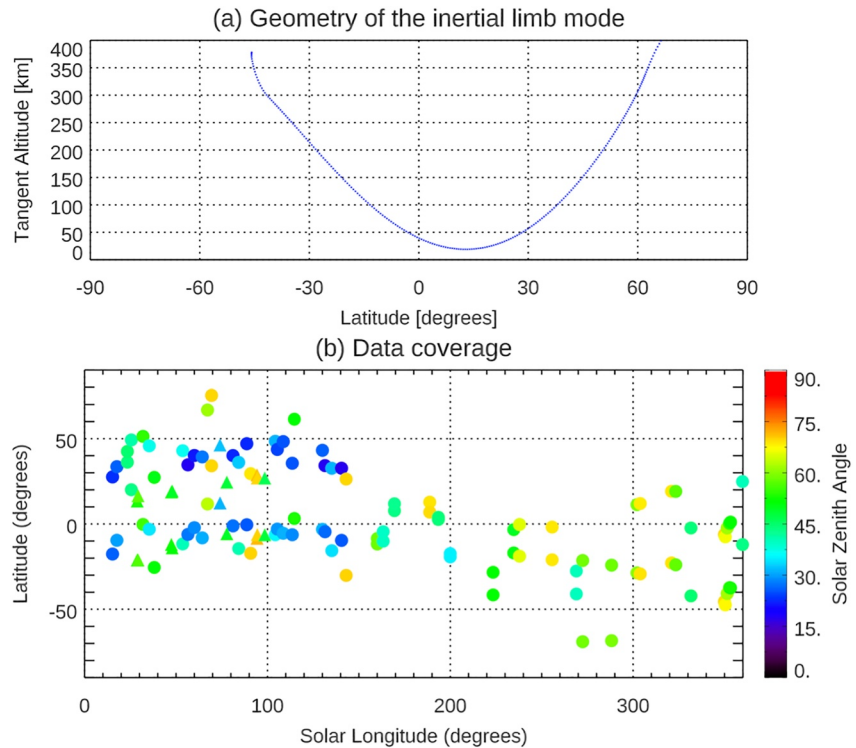


**Figure 1.** (a) Example of the geometry of an inertial limb observation. (b) Solar longitudes ( $x$ -axis) and latitudes ( $y$ -axis) of the Nadir and Occultation for Mars Discovery measurements analyzed in this study. The color denotes the solar zenith angles of the lower peaks. The circle symbols correspond to the data taken in MY35, and the triangle symbols stand for MY36.

typical coverage in latitude and altitude of a single limb orbit obtained by the inertial pointing mode. This mode scans the atmosphere from near-surface to 400 km altitudes twice during each orbit (ingress and egress), typically one in the northern hemisphere and the other one in the southern hemisphere. Operations in this inertial limb mode have been started in April 2019. So far, a total of 90 dayside orbits (solar zenith angle less than  $60^\circ$ ) have been analyzed, Figure 1b shows the seasonal and latitudinal coverage of these 180 limb scans. This data set fully covers Mars Year (MY) 35 and the beginning of MY 36. The latitudes of the measurements are mostly between  $60^\circ\text{N}$  and  $60^\circ\text{S}$ . The local time and longitudes of the measurements are randomly distributed and it is not possible to distinguish between local time and longitudinal variations.

Figure 2a shows an example of a limb spectrum collected by NOMAD/UVIS channel. The OI emission feature is clearly seen at 557.7 nm between 70 and 150 km altitudes. The brightness of the OI emission is calculated at each altitude by the integration of the signal in the spectral range between 556.2 and 559.2 nm. To remove the effect of scattered solar light, a local continuum around the OI emission is first established by using the spectral range between 550.2 and 565.2 nm except 556.2–559.2 nm, and the integral of the differences between the local continuum and measured signal at 556.2–559.2 nm is then calculated. The error values are estimated based on the standard deviation of the signal at the spectral points that are used to establish the local continuum. Figure 2b shows an example of the derived vertical profiles of the OI emission brightness, which typically has two peaks around 80 km (hereafter “lower peak”) and 120 km (hereafter “upper peak”).

## 2.2. Variation of the Peak Intensity and Altitude

Figure 3a shows the variation of the lower peak brightness with the solar zenith angles (SZAs) of the measurements. The peak brightness decreases as the SZA increases. Such a correlation between the OI emission brightness and the SZAs is expected because the lifetime of  $\text{O}(^1\text{S})$  atoms produced by solar EUV photodissociation of  $\text{CO}_2$ , the primary source of the OI emission, is quite short ( $<1\text{s}$ ) and thus the peak brightness directly follows the intensity of the solar EUV flux at the time of measurements (which is primarily controlled by the SZA). Indeed,

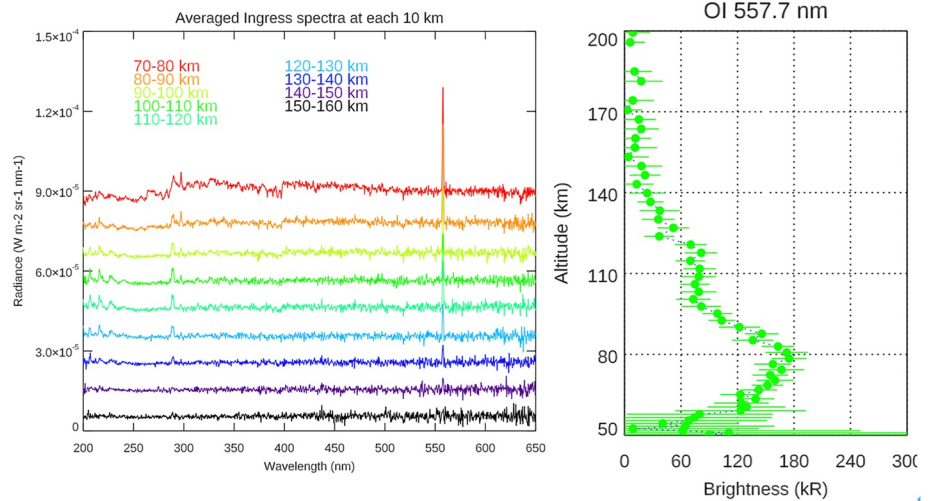


**Figure 2.** (a) Example of the spectra of Nadir and Occultation for Mars Discovery (NOMAD)/Ultraviolet and Visible Spectrometer (UVIS) limb observations taken on 13 September 2021. The spectra are averaged with an interval of 10 km, from 70 to 160 km. The origin of the Y-axis at each altitude below 150 km has been offset to improve visibility. (b) Vertical profile of the oxygen dayglow brightness measured in the NOMAD/UVIS spectra shown in Figure (a).

the measured peak brightness are in good agreement with a  $\cos(SZA)$  function which is shown as the blue curve in Figure 3a.

Figures 3b and 3c show the variation of the lower peak altitudes with seasons (Figure 3b) and latitudes (Figure 3c). Unfortunately, in the middle of MY 35 ( $L_s = 160\text{--}268^\circ$ ), the minimum altitudes of the limb scans

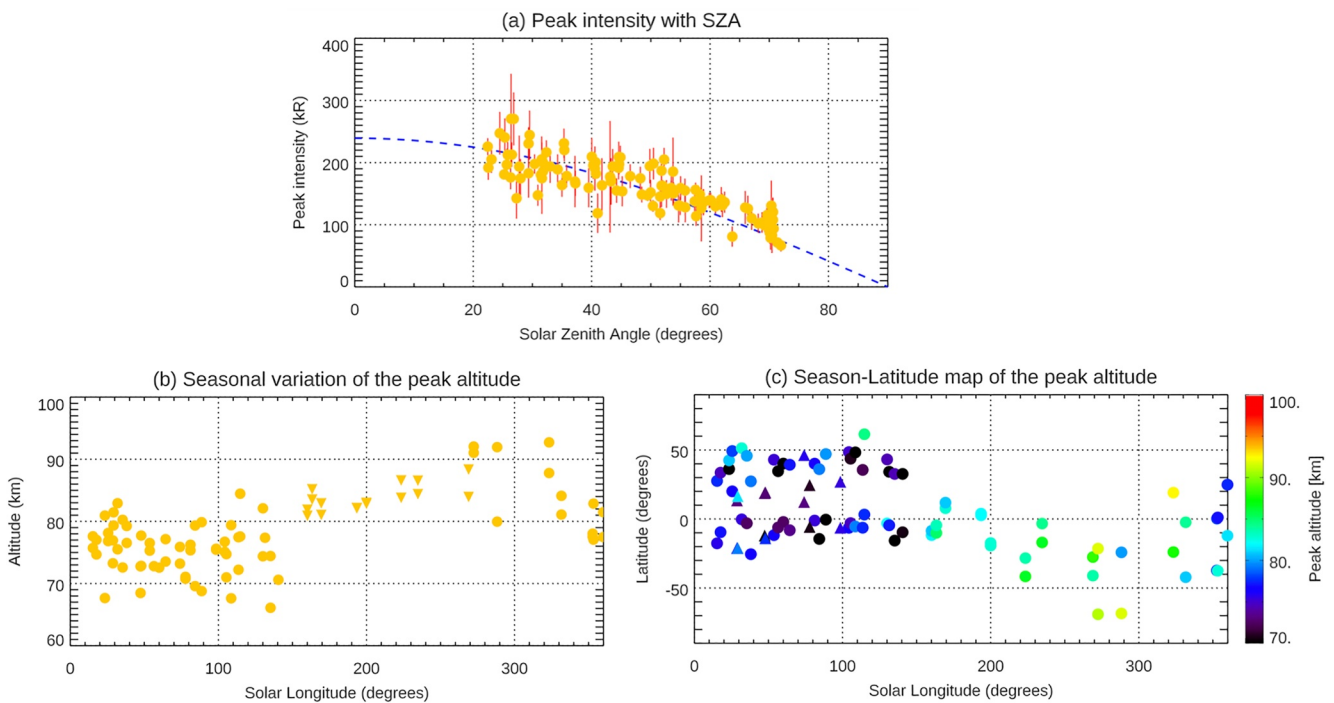


**Figure 3.** (a) Variability of the OI dayglow lower peak intensity with solar zenith angles. The blue curve is  $f(SZA) = 239.26 \times \cos(SZA)$ . (b) Seasonal variation of the OI dayglow lower peak altitudes. The upside-down triangle symbols represent the upper limits of the peak altitudes. (c) Season-latitude maps of the OI dayglow lower peak altitudes. In order to remove the effect of solar zenith angle, the peak altitudes shown in panels (b) and (c) are corrected by the following equation (Gkouvelis, Gérard, González-Galindo, et al., 2020):  $z' = z - \log(1/\cos(\theta)) \times 7.1$ , where  $\theta$  is the solar zenith angle of the measurement,  $z$  is the observed peak altitude, and  $z'$  is the corrected peak altitude that is shown in panels (b) and (c).

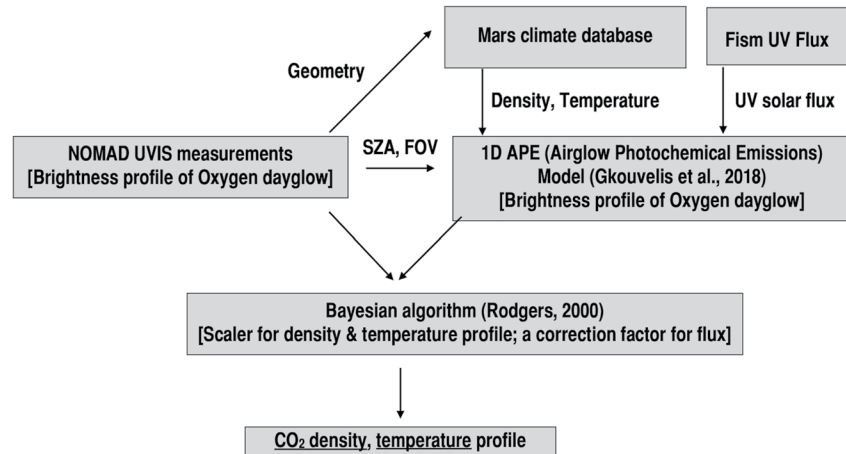


**Figure 4.** Scheme of the retrieval method.

were exceptionally limited to  $\sim 85$  km and thus we can provide only upper limits of the peak altitudes. However, even considering this fact, a significant seasonal variation of the peak altitudes is clearly observed: the peak altitudes have maximum values of  $\sim 90$  km in the southern spring-summer ( $L_s \sim 270^\circ$ ), and minimum value of  $\sim 70$  km in the northern spring-summer ( $L_s \sim 60^\circ$ ). Qualitatively, this suggests that  $\text{CO}_2$  densities are larger in the southern summer than northern summer at the same altitude levels because the peak altitudes are primarily defined by the  $\text{CO}_2$  column abundances above the peaks (Gkouvelis, Gérard, González-Galindo, et al., 2020). In this study, we attempt to quantitatively retrieve the vertical profiles of the densities and temperatures from the OI emission limb profile (see Section 3).

### 3. Retrieval of Density and Temperature

#### 3.1. Retrieval Method

Figure 4 shows the scheme of the retrieval process developed in this study. The core of the inversion scheme is based on the Bayesian algorithm (Rodgers, 2000), which is widely used in non-linear inversion problems in remote-sensing observations of atmosphere (e.g., Grassi et al., 2005; Jiménez-Monferrer et al., 2021). This method iteratively calculates new solutions based on the measurements and a priori information:

$$x_{i+1} = x_i + (S_a^{-1} + K_i^T S_e^{-1} K_i)^{-1} [K_i^T S_e^{-1} (y - F(x_i)) - S_a^{-1} (x_i - x_a)] \quad (1)$$

where  $x$  is a vector of retrieved parameters ( $\text{CO}_2$  density profile, temperature profile, and a factor for flux correction, in this study),  $x_i$  is the solution in the previous iteration,  $x_{i+1}$  is the new solution),  $y$  is a vector of measured limb profile of oxygen dayglow brightness,  $S_e$  is a covariance matrix of measurement errors,  $x_a$  is an a priori vector,  $S_a$  is a covariance matrix of a priori information,  $F(x_i)$  is a vector calculated by the forward model with  $x_i$  (calculated vertical profile of oxygen dayglow brightness), and  $K_i$  is a Jacobian matrix, that is, the partial derivative of the forward model with respect to  $x_i$ ,  $K_i = \partial F / \partial x_i$ .

The forward model  $F(x)$  is calculated by the 1-dimensional photochemical model for airglow emission, named “Photochemical Airglow Mars” (PAM) model (Gérard et al., 2019; Gkouvelis et al., 2018; Gkouvelis, Gérard, Ritter et al., 2020; Ritter et al., 2019), which successfully matched the Ultraviolet lines of O( $^1\text{S}$ ) 297.2 nm, CO Cameron bands,  $\text{CO}_2^+$  UV doublet as well as the green and red optical emission lines at 557 and 630 nm that were discovered at the atmosphere of Mars (Gérard et al., 2020, 2021). This model was originally developed for the oxygen ultraviolet airglow emission of 297.2 nm. Since both OI 557.7 and 297.2 nm forbidden emissions originates from the same oxygen ( $^1\text{S}$ ) upper state, their intensity ratio is equal to that of their transition probability. The two transition probabilities and their ratio  $R = I(557.7 \text{ nm}) / I(297.2 \text{ nm})$  is obtained from ab initio calculations ( $R = 16.7$ ). The PAM model considers all possible sources and losses for the total production of oxygen ( $^1\text{S}$ ) upper state, including its primary source, photodissociation of  $\text{CO}_2$  (see Gkouvelis et al., 2018, in detail). The solar EUV flux at Mars are obtained by FISM-P database (Chamberlin et al., 2007; Thiemann et al., 2017). This

solar EUV flux database is publicly available for the period before 14 Feb. 2020. For the latest period that is not covered by the database, we use the solar EUV flux at the same solar longitude measured during the previous Mars year. A spherical geometry with an onion peeling layers is assumed for the calculation of the optical depth path of each wavelength (Brasseur & Solomon, 1986). To take into account the line-of-sight integration to be compared with the NOMAD limb observations, an algorithm that solves the Abel inverse transformation (Hubert et al., 2022) is used.

The initial guess of the CO<sub>2</sub> density and temperature vertical profile is obtained from the Mars Climate Database (MCD) version 5.3 (Forget et al., 1999; Millour et al., 2018). The retrieved free parameters in this method are the CO<sub>2</sub> density vertical profile, the temperature vertical profile, and a factor for flux correction. The third parameter (a correction factor) is applied to the simulated brightness uniformly in order to correct the calibration of the instrument, solar EUV flux, and residual systematic inaccuracy in the PAM model. The density and temperature profiles are scaled from the a priori MCD profile in each iteration. The sensitivity of the retrieved parameter to the measurement is assessed by an averaging kernel matrix,  $A$ , where  $A = (S_a^{-1} + K^T S_e^{-1} K)^{-1} K^T S_e^{-1} K$ .  $K$  is the Jacobian matrix obtained after the convergence of the iteration. The usefulness of  $A$  is described in Rodgers (2000). In short, each row of  $A$  (hereafter denoted as averaging kernel) represents the sensitivity of the retrieved parameter to the true state. The vertical width of the averaging kernel tells us the vertical resolution of the retrieval. The area of the averaging kernel can be regarded as a measure of the fraction of the information that comes from the measurement, not from the a priori state. We denote this quantity as “measurement response” in this study. The trace of  $A$  is often called as a degree of freedom for the signal, indicating how much vertically resolved parameters can be retrieved from the measurements.

Figure 5 shows an example of the retrieval outputs from a limb profile. Figure 5a illustrates the measured (in green) and best-fit synthetic (in red) vertical profiles of the oxygen dayglow brightness. The agreement between measured and synthetic vertical profiles generally agrees within the 1-sigma uncertainty of the measurements. We note that both the measured and the synthetic vertical profile show two peaks: the lower peak is caused by solar flux of the solar Lyman- $\alpha$  emission at 121.6 nm and the upper peak is produced by solar EUV flux at other wavelengths. Figures 5b-5c and 5d-5e show the Jacobian and averaging-kernel matrices of density and temperature profiles, respectively. In Figures 5d and 5e, the total measurement response, which is calculated by the sum of each kernel, is shown in as the black curves. The degree of freedom is generally about two for density profile and about one for temperature profile. The averaging-kernel matrices suggest that the retrieved density profile contains information only at two altitudes around 90 and 140 km, and the temperature profile has information only one around 80 km altitudes. This limited sensitivity of the density retrieval is consistent with the emission mechanism of the two peaks described above. The temperature retrieval is based on the fact that the quenching coefficient of <sup>1</sup>S oxygen by CO<sub>2</sub>, which is dominant relative to other collisional deactivation processes in the lower thermosphere (Gkouvelis et al., 2018), is temperature dependent. Capetanakis et al. (1993) measured  $k_{CO_2} = (3.21 (\pm 0.25)) \times 10^{-11} e^{-11.0(\pm 0.2)/RT} \text{cm}^{-3} \text{s}^{-1}$ , in full agreement with earlier measurements by Atkinson and Welge (1972). We note that the temperature dependence of the quenching coefficient was measured between 200 and 470 K (Capetanakis et al., 1993). We take advantage of this dependence and assume that this expression may be extrapolated down to Mars atmospheric temperature (down to 100 K). Figures 5f and 5g and Figures 5h and 5i show the retrieved CO<sub>2</sub> density and temperature profiles. The scaler relative to the initial profile from MCD is presented in Figures 5d and 5h, and the absolute CO<sub>2</sub> number density and temperature are presented in Figures 5e and 5i. The smallest error in the retrieved CO<sub>2</sub> density profile is about 20% relative to the MCD initial guess around 90 km altitude. Figure 5i is the retrieved temperature profile. The error in the retrieved temperature is relatively large, about  $\pm 40$  K. It is noted that the retrieved temperature and the errors shown in Figure 5i are meaningful only at the altitude around 80 km.

The retrievals have been applied to all of the NOMAD inertial limb observations (180 scans). However, as discussed above, despite the fact that retrievals are done for the whole altitude between 50 and 200 km, only one or two atmospheric layers contain the proper information. We thus apply the following criteria to pick up the valid retrievals:

1. Solar zenith angle of the lower peak is less than 60° since the dayglow brightness of the data with higher SZAs is not strong enough (thus low signal-to-noise ratio);

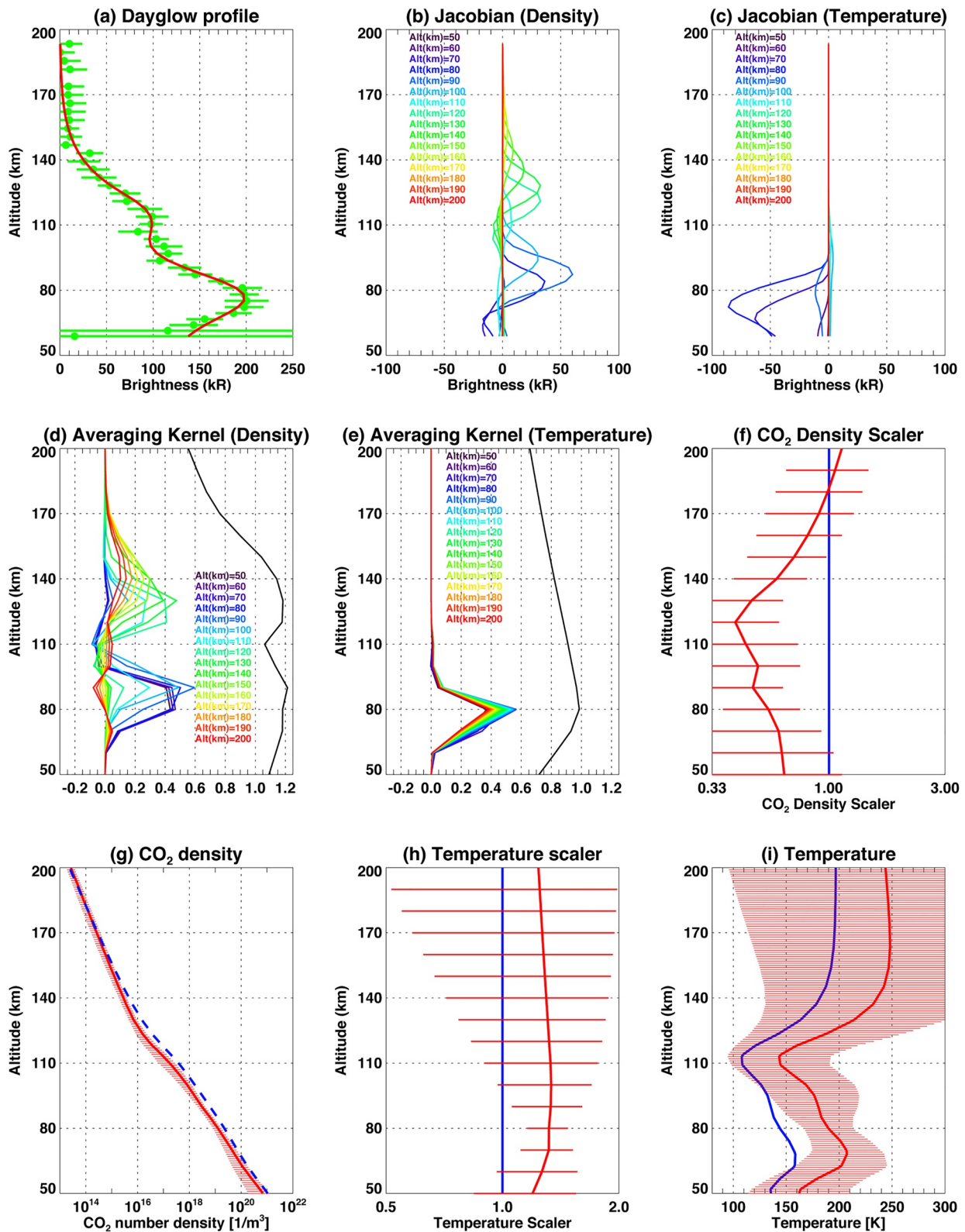
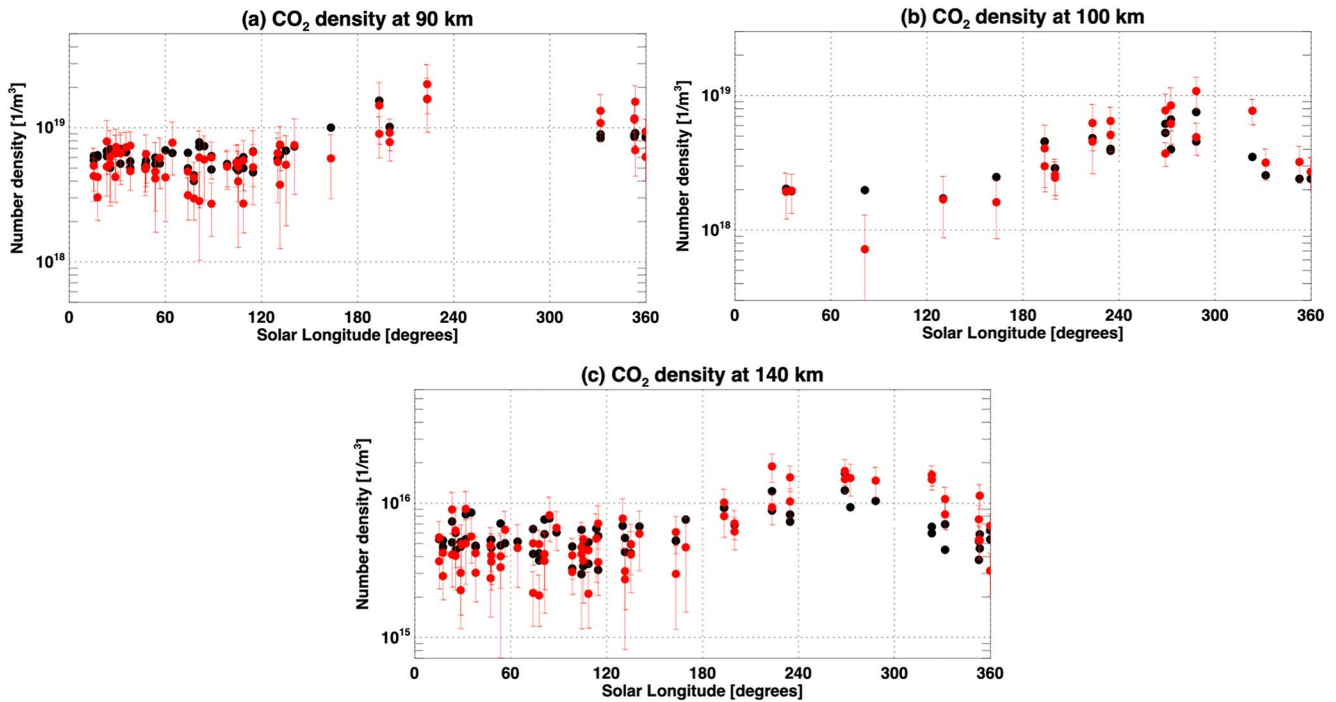


Figure 5.



**Figure 6.** Seasonal variation of the CO<sub>2</sub> density (red) at 90 km (a), 100 km (b), and 140 km (c). The black points are the CO<sub>2</sub> density predicted by MCD that are used as a priori value.

2. More than 2/3 of the retrieved information comes from an appropriate altitude for a retrieved parameter. That is, the amplitude of the averaging kernel at the appropriate altitude is larger than 2/3 of the maximum value of that kernel;
3. Retrieved information that comes from the measurements is larger than that from the a priori. Namely, the measurement response is greater than 0.5.

In the following section, only the results meeting by these criteria are considered.

### 3.2. Density Variation

Figures 6a–6c show the seasonal variation of the retrieved CO<sub>2</sub> density at 90 km (Figure 6a), at 100 km (Figure 6b), and at 140 km altitude (Figure 6c). The red points in these figures are the retrieved densities and the black points are a priori densities obtained from MCD. The sensitive altitude is different and depends on season, thus the solar longitudes of the shown densities are different at 90 and 100 km. Clear seasonal trends are found in the retrieved CO<sub>2</sub> densities as well as in the a priori densities at whole altitudes. In order to confirm that the information of the retrieved densities are not driven by the MCD a priori profile but from the NOMAD measurements, we performed the same analysis starting from the annual-averaged CO<sub>2</sub> density of MCD profile as a priori (i.e., the same “mean” profile is used for the all of the retrievals). Figures 7a–7c show the results of this test at 90 km, 100 km, and 140 km. The retrieved CO<sub>2</sub> densities starting from the annual-averaged density show very similar seasonal variations to the ones using individual MCD profile as a priori, which demonstrates that the information of the retrieved CO<sub>2</sub> densities actually originate from the NOMAD measurements.

**Figure 5.** Example of the outputs from the retrieval analysis. (a) The vertical profiles of the OI dayglow brightness measured by Nadir and Occultation for Mars Discovery (NOMAD)/Ultraviolet and Visible Spectrometer (UVIS) and calculated by the model with the retrieved best-fit parameters (the red curve). (b) Jacobian matrix for density scaler. Each profile shows the sensitivity of the vertical profile of the dayglow brightness with respect to the CO<sub>2</sub> density scaler for specific altitude (labeled in the legend). (c) Jacobian matrix for temperature scaler. (d) Averaging kernel matrix for density scaler. (e) Averaging kernel matrix for temperature scaler. Black curves in Figures. (d) and (e) present the total measurement response. (f) Retrieved CO<sub>2</sub> density in the unit of scaler with 1- $\sigma$  retrieval errors (red) relative to the initial vertical profile given by MCD (blue). (g) Retrieved CO<sub>2</sub> density in the unit of number density from NOMAD/UVIS (red), and the a priori CO<sub>2</sub> number density given by MCD (blue). (h) Retrieved temperature in the unit of scaler. (i) Retrieved temperature in the unit of Kelvin from NOMAD/UVIS (red), and the a priori temperature given by MCD (blue).



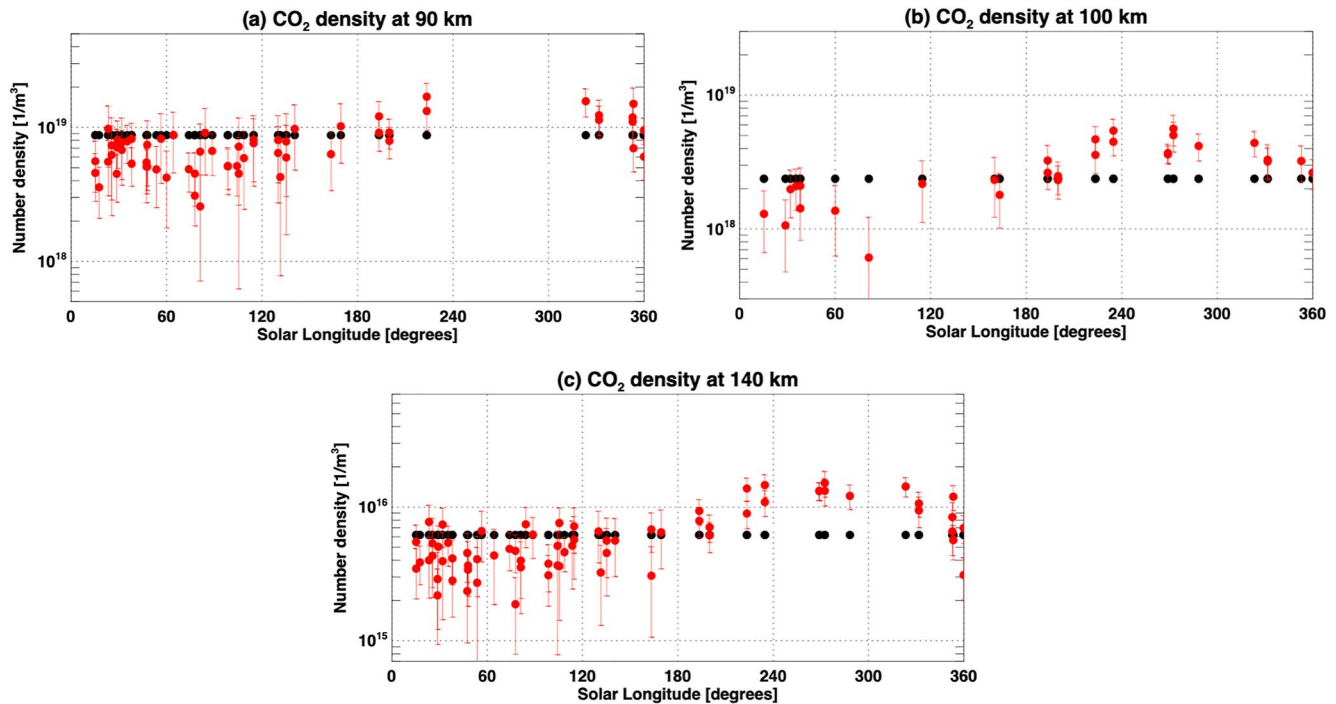


Figure 7. Same as Figure 6 but a priori is the annual-averaged MCD value.

The retrieved CO<sub>2</sub> densities at 90 km, 100 km, and 140 km show a similar seasonal trend, which have maximum values of  $\sim 2 \times 10^{19} \text{ m}^{-3}$  at 90 km,  $\sim 1 \times 10^{19} \text{ m}^{-3}$  at 100 km, and  $\sim 2 \times 10^{16} \text{ m}^{-3}$  at 140 km in perihelion, and minimum values of  $\sim 3 \times 10^{18} \text{ m}^{-3}$  at 90 km,  $\sim 7 \times 10^{17} \text{ m}^{-3}$  at 100 km, and  $\sim 2 \times 10^{15} \text{ m}^{-3}$  at 140 km near aphelion. These absolute values are consistent with the previous measurements (Forget et al., 2009; Gröller et al., 2018; Montmessin et al., 2017) and the values predicted by MCD. The seasonal variation of the CO<sub>2</sub> densities obtained from the NOMAD data is also very similar to the results of the analysis of the SPICAM/UV and MAVEN/IUVS measurements (Forget et al., 2009; Gröller et al., 2018; Montmessin et al., 2017). This seasonal variation can be explained by the relatively short distance between Mars and the Sun during the southern spring-summer that heats up the lower atmosphere and raises dust in the atmosphere (which also heats the atmosphere). Consequently, the atmosphere “expands” during this period of the year - in other words, the combination between dust content in the lower atmosphere and Sun-Mars distance controls the density in the upper atmosphere (Forget et al., 2009; McDunn et al., 2010).

### 3.3. Temperature Variation

Figures 8a–8d show the variability of the retrieved temperature at 80 km versus season (Figure 8a), local solar time (Figure 8b), latitude (Figure 8c), and longitude (Figure 8d). Even though the error values are relatively large (about  $\pm 40 \text{ K}$ ), the retrieved temperature (the global mean value:  $173 \pm 27 \text{ K}$ ) is systematically higher than those predicted by MCD (the global mean value:  $147 \pm 7 \text{ K}$ ). From this data set, it is not possible to distinguish among seasonal, latitudinal, longitudinal, and local time variations. However, it is suggested that temperature is slightly higher in the northern spring-summer (the mean value:  $182 \pm 23 \text{ K}$  at  $L_s = 0\text{--}120^\circ$ ) than those in the rest of the year, and/or in the morning (the mean value:  $191 \pm 18 \text{ K}$  in 8–9 hr). The latitudes of the retrieved temperature are mostly within  $\pm 50^\circ$ , and we do not find any particular latitudinal and longitudinal variations.

Recently, analysis of nightside temperature profiles in the UMLT region retrieved from MAVEN/IUVS stellar occultations revealed a surprising enhancement (so-called “warm layer”) of up to 90 K above the previous model predictions at altitudes  $\sim 80 \text{ km}$  (Nakagawa et al., 2020). The high daytime temperature around 80 km observed by NOMAD/UVIS could suggest that such a warm layer might be present in daytime. However, as described above, this analysis is limited to only one altitude and therefore the observed high temperature could be either consistent with a warm layer in daytime, or alternatively due to a systematic error in the retrieval. As described

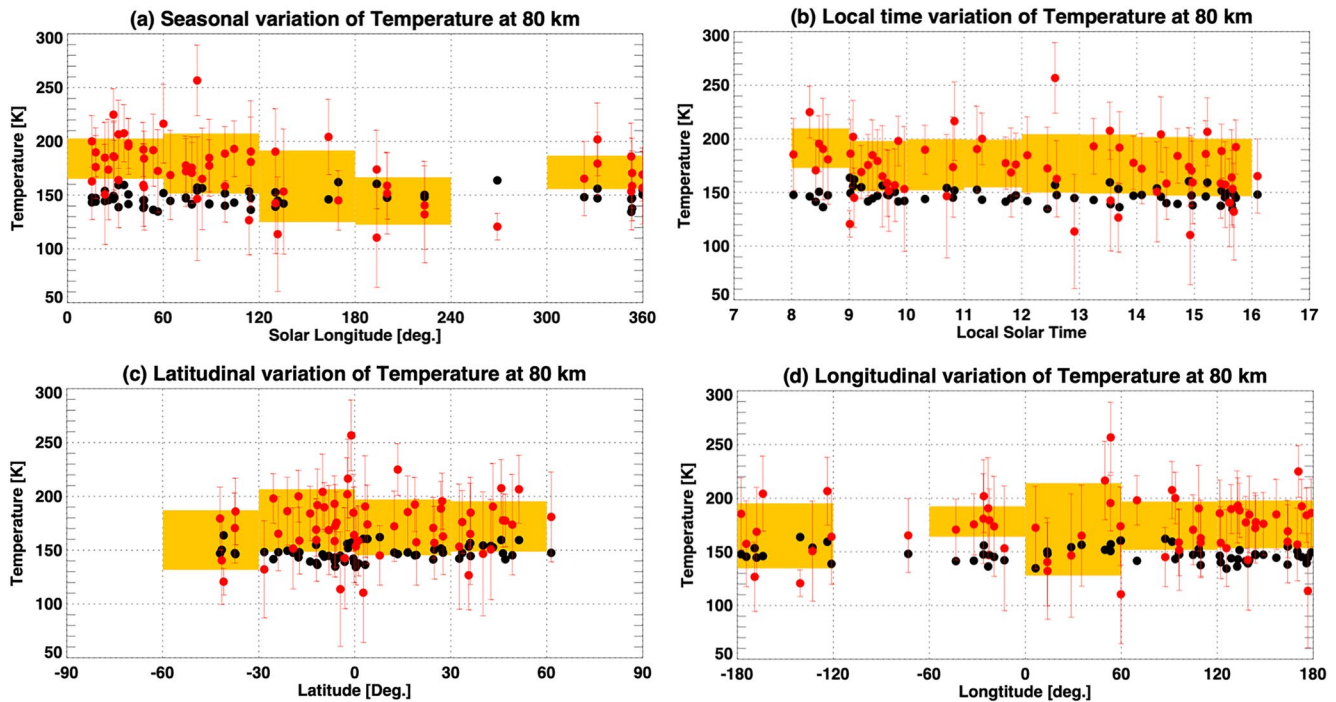


**Figure 8.** Variability of the retrieved temperature (red points) at 80 km in season (a), local time (b), latitude (c), and longitude (d). The black points are the temperatures predicted by the MCD that are used as a priori value. The orange shadows show the average and standard deviation of the corresponding zones.

in Section 3.1, the temperature retrieval relies on the temperature dependence of the quenching coefficient of  $^1\text{S}$  oxygen by  $\text{CO}_2$ . The uncertainty in the quenching coefficient ( $k_{\text{CO}_2} = (3.21 (\pm 0.25)) \times 10^{-11} e^{-11.0(\pm 0.2)/RT} \text{cm}^{-3} \text{s}^{-1}$ ) leads systematic error of about  $\pm 5$  K in the retrieved temperature. This is much smaller than the difference between measured temperature and GCM predictions, which supports that the retrieved higher temperature is true. However, the valid temperature range of the equation is between 210 and 450 K so that we cannot rule out the possibility that the retrieved temperature could be biased by the assumption that the  $k_{\text{CO}_2}$  expression can be extrapolated down to 100 K. A further experimental verification of the equation in the range of Mars upper atmosphere is required to confirm the measured high temperature.

The analysis of the slope of the oxygen dayglow profile at 297.2 nm with MAVEN/IUVS by Jain et al. (2021) discussed the temperature around  $\sim 90$ – $105$  km and is thus not directly comparable to the present results. However, the suggested temperatures at  $\sim 90$ – $105$  km are mostly between 120 and 160 K. These are significantly lower than the observed temperature at 80 km, which is consistent with the presence of the warm atmospheric layer.

#### 4. Conclusions

This study demonstrates that oxygen dayglow emitted at 557.7 nm is a good tracer to investigate the climatology of the upper mesosphere and lower thermosphere of Mars (UMLT70–150 km altitude). The combined use of the 1-D PAM model and widely used Bayesian inversion algorithm allows us to retrieve density around 90, 100 and 140 km and temperature around 80 km from the oxygen dayglow acquired by TGO/NOMAD limb observations. We found that retrieved daytime densities at 90, 100 and 140 km have a significant seasonal variation, which is controlled by temperature and dust content in the lower atmosphere. Such variations have already been found during nighttime by MEx/SPICAM (Forget et al., 2009; Montmessin et al., 2017) and partially in daytime by MAVEN/IUVS (Gröller et al., 2018). This TGO/NOMAD analysis supports those findings with a full seasonal coverage in daytime through a Mars year. The temperature retrieval is sensitive to only a limited altitude range around 80 km, and its uncertainty is limited to  $\pm 40$  K. However, it is suggested that the temperature at 80 km in daytime is higher than the GCM predictions. It is tentatively consistent with the warm atmospheric layer recently discovered in nightside. For the verification of the retrieved high temperature, further experimental studies are needed to quantify the quenching coefficient of  $^1\text{S}$  oxygen by  $\text{CO}_2$  at the temperature range of the Mars upper

atmosphere. Another limitation of this analysis is its poor vertical resolution. This can be improved by combining with other dayglow emissions (such as the  $\text{CO}_2^+$  UV doublet) in the future.

## Data Availability Statement

The results retrieved from the NOMAD measurements used in this article are available on the BIRA-IASB data repository: <https://repository.aeronomie.be/?doi=10.18758/71021073> (Aoki & Vandaele, 2022). The NOMAD spectra are available from ESA's Planetary Science Archive at <https://archives.esac.esa.int/psa/#!/Table%20View/NOMAD=instrument>.

## Acknowledgments

The NOMAD experiment is led by the Royal Belgian Institute for Space Aeronomy (IASB-BIRA), assisted by Co-PI teams from Spain (IAA-CSIC), Italy (INAF-IAPS), and the United Kingdom (The Open University). This project acknowledges funding by the Belgian Science Policy Office (BELSPO), with the financial and contractual coordination by the ESA Prodex Office (PEA 4000103401, 4000121493), by the Spanish Ministry of Science and Innovation (MCIU) and by European funds under grants PGC2018-101836-B-I00 and ESP2017-87143-R (MINECO/FEDER), as well as by UK Space Agency through grants ST/V002295/1, ST/V005332/1 and ST/S00145X/1 and Italian Space Agency through Grant 2018-2-HH.0. This work was supported by the Belgian Fonds de la Recherche Scientifique – FNRS under Grant No. 30442502 (ET\_HOME). The IAA/CSIC team acknowledges financial support from the State Agency for Research of the Spanish MCIU through the “Center of Excellence Severo Ochoa” award for the Instituto de Astrofísica de Andalucía (SEV-2017-0709). US investigator was supported by the National Aeronautics and Space Administration. F.G.-G. is funded by the Spanish Ministerio de Ciencia, Innovación y Universidades, the Agencia Estatal de Investigación and EC FEDER funds under project RTI2018-100920-J-I00.

## References

- Aoki, S., & Vandaele, A. C. (2022). *Density and temperature of the upper mesosphere and lower thermosphere of Mars retrieved from the OI 557.7 nm dayglow measured by TGO/NOMAD, presented in Aoki et al.* Royal Belgian Institute for Space Aeronomy. <https://doi.org/10.18758/71021073>
- Atkinson, R., & Welge, K. H. (1972). Temperature dependence of O (<sup>1</sup>S) deactivation by CO<sub>2</sub>, O<sub>2</sub>, N<sub>2</sub>, and Ar. *The Journal of Chemical Physics*, 57(9), 3689–3693. <https://doi.org/10.1063/1.1678829>
- Bougher, S. W., Brain, D. A., Fox, J. L., Gonzalez-Galindo, F., Simon-Wedlund, C., & Withers, P. G. (2017). Chapter 14: Upper neutral atmosphere and ionosphere. In B. Haberle, M. Smith, T. Clancy, F. Forget, & R. Zurek (Eds.), *The atmosphere and climate of Mars*. Cambridge University Press. <https://doi.org/10.1017/9781107016187>
- Brasseur, G., & Solomon, S. (1986). *Aeronomy of the middle atmosphere* (2nd ed.). D. Reidel.
- Capetanakis, F. P., Sondermann, F., Höser, S., & Stuhl, F. (1993). Temperature dependence of the quenching of O(<sup>1</sup>S) by simple inorganic molecules. *The Journal of Chemical Physics*, 98(10), 7883–7887. <https://doi.org/10.1063/1.464596>
- Chamberlain, P. C., Woods, T. N., & Eparvier, F. G. (2007). Flare irradiance spectral model (FISM): Daily component algorithms and results. *Space Weather*, 5(7). <https://doi.org/10.1029/2007SW000372>
- Forget, F., Hourdin, F., Fournier, R., Hourdin, C., Talagrand, O., Collins, M., et al. (1999). Improved general circulation models of the Martian atmosphere from the surface to above 80 km. *Journal of Geophysical Research*, 104(E10), 24155–24176. <https://doi.org/10.1029/1999JE001025>
- Forget, F., Montmessin, F., Bertaux, J. L., González-Galindo, F., Lebonnois, S., Quemerais, E., et al. (2009). Density and temperatures of the upper Martian atmosphere measured by stellar occultations with Mars express SPICAM. *Journal of Geophysical Research*, 114(E1), E01004. <https://doi.org/10.1029/2008JE003086>
- Gérard, J. C., Aoki, S., Gkouvelis, L., Soret, L., Willame, Y., Thomas, I. R., et al. (2021). First observation of the oxygen 630 nm emission in the Martian dayglow. *Geophysical Research Letters*, 48(8), e2020GL092334. <https://doi.org/10.1029/2020gl092334>
- Gérard, J. C., Aoki, S., Ritter, B., Willame, Y., Hubert, B., Gkouvelis, L., et al. (2020). Detection of green line emission in the dayside atmosphere of Mars from NOMAD-TGO observations. *Nature Astronomy*, 124(7), 5–8. <https://doi.org/10.1029/2019JA026596>
- Gérard, J. C., Gkouvelis, L., Ritter, B., Hubert, B., Jain, S. K., & Schneider, N. M. (2019). MAVEN-IUVS observations of the CO<sub>2</sub><sup>+</sup> UV doublet and CO Cameron bands in the Martian thermosphere: Aeronomy, seasonal, and latitudinal distribution. *Journal of Geophysical Research: Space Physics*, 124(7), 5816–5827. <https://doi.org/10.1029/2019ja026596>
- Gkouvelis, L., Gérard, J. C., González-Galindo, F., Hubert, B., & Schneider, N. M. (2020). Isobar altitude variations in the upper mesosphere observed with IUVS-MAVEN in response to martian dust storms. *Geophysical Research Letters*, 47(12), e2020GL087468. <https://doi.org/10.1029/2020gl087468>
- Gkouvelis, L., Gérard, J.-C., Ritter, B., Hubert, B., Schneider, N. M., & Jain, S. K. (2018). The O(<sup>1</sup>S) 297.2-nm dayglow emission: A tracer of CO<sub>2</sub> density variations in the martian lower thermosphere. *Journal of Geophysical Research: Planets*, 123(12), 3119–3132. <https://doi.org/10.1029/2018JE005709>
- Gkouvelis, L., Gérard, J. C., Ritter, B., Hubert, B., Schneider, N. M., & Jain, S. K. (2020). Airglow remote sensing of the seasonal variation of the martian upper atmosphere: MAVEN limb observations and model comparison. *Icarus*, 341, 113666. <https://doi.org/10.1016/j.icarus.2020.113666>
- Grassi, D., Ignatiev, N. I., Zasova, L. V., Maturilli, A., Formisano, V., Bianchini, G. A., & Giuranna, M. (2005). Methods for the analysis of data from the planetary Fourier Spectrometer on the Mars express mission. *Planetary and Space Science*, 53(10), 1017–1034. <https://doi.org/10.1016/j.pss.2005.01.006>
- Gröller, H., Montmessin, F., Yelle, R. V., Lefèvre, F., Forget, F., Schneider, N. M., et al. (2018). MAVEN/IUVS stellar occultation measurements of Mars atmospheric structure and composition. *Journal of Geophysical Research: Planets*, 123(6), 1449–1483. <https://doi.org/10.1029/2017JE005466>
- Hubert, B., Munhoven, G., Moulane, Y., Hutsemekers, D., Manfroid, J., Opitom, C., & Jehin, E. (2022). Analytic and numerical methods for the Abel transform of exponential functions for planetary and cometary atmospheres. *Icarus*, 371, 114654. <https://doi.org/10.1016/j.icarus.2021.114654>
- Jain, S. K., Soto, E., Evans, J. S., Deighan, J., Schneider, N. M., & Bougher, S. W. (2021). Thermal structure of Mars middle and upper atmospheres: Understanding the impacts of dynamics and of solar forcing. *Icarus*. in press. <https://doi.org/10.1016/j.icarus.2021.114703>
- Jiménez-Monferrer, S., López-Valverde, M. Á., Funke, B., González-Galindo, F., Piccialli, A., García-Comas, M., et al. (2021). CO<sub>2</sub> retrievals in the Mars daylight thermosphere from its 4.3 μm limb emission measured by OMEGA/MEX. *Icarus*, 353, 113830. <https://doi.org/10.1016/j.icarus.2020.113830>
- Keating, G. M., Bougher, S. W., Zurek, R. W., Tolson, R. H., Cancro, G. J., Noll, S. N., et al. (1998). The structure of the upper atmosphere of Mars: In situ accelerometer measurements from Mars Global Surveyor. *Science*, 279(5357), 1672–1676. <https://doi.org/10.1126/science.279.5357.1672>
- López-Valverde, M. A., Gérard, J.-C., González-Galindo, F., Vandaele, A. C., Thomas, I., Korabev, O., et al. (2018). Investigations of the Mars upper atmosphere with ExoMars trace gas orbiter. *Space Science Reviews*, 214(1), 29. <https://doi.org/10.1007/s11214-017-0463-4>
- Magalhães, J. A., Schofield, J. T., & Seiff, A. (1999). Results of the Mars Pathfinder atmospheric structure investigation. *Journal of Geophysical Research*, 104(E4), 8943–8956. <https://doi.org/10.1029/1998JE900041>

- McDunn, T., Bougher, S. W., Murphy, J., Smith, M. D., Forget, F., Bertaux, J.-L., & Montmessin, F. (2010). Simulating the density and thermal structure of the middle atmosphere (80–130 km) of Mars using the MGCM-MTGCM: A comparison with MEX-SPICAM observations. *Icarus*, 206(1), 5–17. <https://doi.org/10.1016/j.icarus.2009.06.034>
- Millour, E., Forget, F., Spiga, A., Vals, M., Zakharov, V., Montabone, L., et al. (2018). The Mars climate database (version 5.3). In *Proceedings of the Mars science workshop "from Mars express to ExoMars"*. ESAC. Retrieved from <https://www.cosmos.esa.int/web/mars-science-workshop-2018>
- Montmessin, F., Korablev, O., Lefèvre, F., Bertaux, J.-L., Fedorova, A., Trokhimovskiy, A., et al. (2017). SPICAM on Mars express: A 10 year in-depth survey of the martian atmosphere. *Icarus*, 297, 195–216. <https://doi.org/10.1016/j.icarus.2017.06.022>
- Nakagawa, H., Jain, S. K., Schneider, N. M., Montmessin, F., Yelle, R. V., Jiang, F., et al. (2020). A warm layer in the nightside mesosphere of Mars. *Geophysical Research Letters*, 47(4), e85646. <https://doi.org/10.1029/2019GL085646>
- Patel, M. R., Antoine, P., Mason, J., Leese, M., Hathi, B., Stevens, A. H., et al. (2017). NOMAD spectrometer on the ExoMars trace gas orbiter mission: Part 2—Design, manufacturing, and testing of the ultraviolet and visible channel. *Applied Optics*, 56(10), 2771–2782. <https://doi.org/10.1364/AO.56.002771>
- Ritter, B., Gérard, J.-C., Gkouvelis, L., Hubert, B., Jain, S. K., & Schneider, N. M. (2019). Characteristics of Mars UV dayglow emissions from atomic oxygen at 130.4 and 135.6 nm: MAVEN/IUVS limb observations and modeling. *Journal of Geophysical Research: Space Physics*, 124(6), 4809–4832. <https://doi.org/10.1029/2019JA026669>
- Rodgers, C. D. (2000). Inverse methods for atmospheric sounding - Theory and practice. In C. D. Rodgers (Ed.), *Inverse methods for atmospheric sounding - theory and practice, series: Series on atmospheric oceanic and planetary physics* (Vol. 2). World Scientific Publishing Co. Pte. Ltd. (ISBN: 9789812813718). <https://doi.org/10.1142/9789812813718>
- Seiff, A., & Kirk, D. B. (1977). Structure of the atmosphere of Mars in summer mid-latitudes. *Journal of Geophysical Research*, 82(28), 4364–4378. <https://doi.org/10.1029/JS082i028p04364>
- Starichenko, E. D., Belyaev, D. A., Medvedev, A. S., Fedorova, A. A., Korablev, O. I., Trokhimovskiy, A., et al. (2021). Gravity wave activity in the Martian atmosphere at altitudes 20–160 km from ACS/TGO occultation measurements. *Journal of Geophysical Research: Planets*, 126(8), e2021JE006899. <https://doi.org/10.1029/2021JE006899>
- Thiemann, E. M., Chamberlin, P. C., Eparvier, F. G., Templeman, B., Woods, T. N., Bougher, S. W., & Jakosky, B. M. (2017). The MAVEN EUVM model of solar spectral irradiance variability at Mars: Algorithms and results. *Journal of Geophysical Research: Space Physics*, 122(3), 2748–2767. <https://doi.org/10.1002/2016JA023512>
- Vandaele, A. C., Lopez-Moreno, J.-J., Patel, M. R., Bellucci, G., Daerden, F., Ristic, B., et al. (2018). NOMAD, an integrated suite of three spectrometers for the ExoMars trace gas mission: Technical description, science objectives and expected performance. *Space Science Reviews*, 214(5), 80. <https://doi.org/10.1007/s11214-018-0517-2>
- Vandaele, A. C., Willame, Y., Depiesse, C., Thomas, I., Robert, S., Bolsée, D., et al. (2015). Optical and radiometric models of the NOMAD instrument part I: The UVIS channel. *Optics Express*, 23(23), 30028–30042. <https://doi.org/10.1364/OE.23.030028>
- Withers, P., & Smith, M. D. (2006). Atmospheric entry profiles from the Mars exploration rovers spirit and opportunity. *Icarus*, 185(1), 133–142. <https://doi.org/10.1016/j.icarus.2006.06.013>